

Rotary Scanning Acquisition in Ultra-Low-Field MRI

Yi-Cheng Hsu,¹ Koos C.J. Zevenhoven,² Ying-Hua Chu,¹ Juhani Dabek,²
Risto J. Ilmoniemi,² and Fa-Hsuan Lin^{1,2*}

Purpose: To develop a method of achieving large field of view (FOV) imaging with a smaller amount of data in ultra-low-field (ULF) MRI.

Theory: In rotary scanning acquisition (RSA), data from the imaging object is acquired at multiple angles by rotating the object or the scanner. RSA is similar to radial-trajectory acquisition but simplifies the measurement and image reconstruction when concomitant fields are nonnegligible.

Methods: RSA was implemented to achieve large FOV with only three localized superconductive quantum interference device (SQUID) sensors at the ULF-MRI field of 50 μ T.

Results: Simulations suggest benefits of RSA, including reduced concomitant field artifacts, large FOV imaging, and SNR improvement. Experimental data demonstrate the feasibility of reconstructing large FOV images using only three SQUID sensors with 33% of the amount of data collected using a Cartesian trajectory.

Conclusion: RSA can be useful in low-field, low-weight, or portable MRI to generate large FOV images with only a few sensors. **Magn Reson Med** 75:2255–2264, 2016. © 2015 Wiley Periodicals, Inc.

Key words: RSA; radial trajectory; rotation; SENSE; ULF MRI; concomitant effect; SNR

INTRODUCTION

MRI has become an indispensable tool in clinical diagnosis and neuroscience studies. Because of the resulting higher signal-to-noise ratio (SNR) (1), higher magnetic fields have been the trend in MRI development, with the proton Larmor frequency up to hundreds of MHz. Differently, ultra-low-field (ULF) MRI uses a magnetic field in the microtesla range for nuclear magnetization precession with Larmor precession frequencies of only thousands of Hz (2). Although the ULF-MRI signal is weaker, there are

many compelling reasons for operating MRI at a relatively weak magnetic field: ULF MRI can provide acoustically silent acquisition, low projectile danger, safe operation, imaging compatibility with metal objects, and an MRI system with open access. In addition, there is evidence that the T_1 contrast between healthy (3) and malignant (4) tissues is higher in sub-millitesla magnetic fields than in the tesla range. Image distortion due to susceptibility can also be greatly reduced in ULF MRI. However, ULF MRI suffers from low SNR, which can be partially improved by using a separate and relatively strong prepolarization field (2) and by sensitive magnetic-field detectors, such as those based on superconductive quantum interference devices (SQUIDs). An ULF-MRI system using SQUIDs for signal detection also gives the opportunity to measure extremely weak biomagnetic fields, such as those in magnetoencephalography (MEG). Thus, combining ULF-MRI and MEG as a single instrument is promising (5,6), because this combination will allow simultaneous anatomical and millisecond-scale functional imaging of the human brain. It has been expected that an integrated ULF-MRI and MEG system can reduce the co-registration error to be as low as 1 mm (6).

One practical challenge in developing an ULF-MRI system is that the SQUID sensors need to recover quickly after the prepolarizing field pulse (7). While we can place SQUID sensors carefully to avoid the penetration of the prepolarization field through the sensors, such an arrangement makes it difficult to arrange sensors such that a large field-of-view (FOV) is imaged homogeneously. Another challenge of ULF MRI is the image distortion and blurring caused by concomitant fields (4,8–10), if images are reconstructed assuming that the magnetic fields generated by gradients are perfectly linear and have only the z-component.

Here, we propose the rotary scanning acquisition (RSA) method, which was applied to ULF MRI to mitigate the challenges described above. In RSA, data from the sample is acquired at multiple angles by rotating the sample or the instrument, *without* any phase encoding. Closely related to radial-trajectory acquisition (11), RSA is expected to improve the SNR per unit time, because the k-space sampling in RSA is denser at low spatial frequencies than at high spatial frequencies. This feature also suggests that RSA, like radial-trajectory acquisition, can have better quality using fewer data samples than Cartesian trajectory acquisition (12). Different from the radial-trajectory acquisition, where careful measurement of the concomitant field across rotation angles and complicated postprocessing methods (13–15) are needed to reduce image blurring and distortion artifacts in ULF MRI, RSA can reduce the image distortion and blurring

¹Institute of Biomedical Engineering, National Taiwan University, Taipei, Taiwan.

²Department of Biomedical Engineering and Computational Science, Aalto University School of Science, Espoo, Finland.

Grant sponsor: NSC; Grant number: 101-2628-B-002-005-MY3; Grant sponsor: Ministry of Science and Technology, Taiwan; Grant number: MOST 103-2628-B-002-002-MY3; Grant sponsor: Ministry of Health and Welfare; Grant number: MOHW103-TDU-PB-211-000026; Grant sponsor: National Health Research Institute, Taiwan, Taiwan; Grant number: NHRI-EX103-10247EI; Grant sponsor: Finland Distinguished Professor (Fidipro) program (TEKES); Grant sponsor: the Finnish Cultural Foundation; Grant sponsor: the Academy of Finland.

*Correspondence to: Fa-Hsuan Lin, Ph.D., Institute of Biomedical Engineering, National Taiwan University, 1 Section 4, Roosevelt Road, Taipei, 106 Taiwan. E-mail: fhlin@ntu.edu.tw

Received 2 October 2014; revised 6 February 2015; accepted 6 February 2015

DOI 10.1002/mrm.25676

Published online 30 June 2015 in Wiley Online Library (wileyonlinelibrary.com).

© 2015 Wiley Periodicals, Inc.

caused by the concomitant field without tedious calibration measurements, because concomitant fields do not change between rotation angles in RSA. Using empirical data, we demonstrate that RSA can generate a full-FOV image using 33% of the amount of data collected by the conventional Fourier encoding method with only three localized SQUID sensors. The RSA method holds promise for a portable imaging system using only frequency-encoding gradients and a small number of NMR signal detectors.

THEORY

In RSA, ULF-MRI data are collected by repeating the process of (i) acquiring frequency-encoded data and (ii) changing incrementally the angle of the sample with respect to the frame of the scanner. Therefore, both the spatial encoding magnetic fields generated by gradient coils and the coil sensitivity experienced by the sample change across measurements. To simplify the following discussion, we assume that two-dimensional (2D) imaging is performed on the x - z plane. Accordingly, the signal in one read-out using the frequency encoding gradient in along the x -axis at frequency ω_l when the imaging object is rotated at θ_n from the x -axis is:

$$S_{\text{RSA}}^m(\omega_l, \theta_n) = \int_{\mathbf{R}} \rho(x \cos(\theta_n) - z \sin(\theta_n), -x \sin(\theta_n) - z \cos(\theta_n)) C_m(x, z) \text{sinc}\left(\frac{\omega(x, z) - (l - L/2)\Delta\omega - \omega_0}{\Delta\omega}\right) dx dz \quad [1]$$

where $S_{\text{RSA}}^m(\omega_l, \theta_n)$ is the signal acquired by the m^{th} receiving coil at frequency ω_l . $\omega(x, z)$ is the magnetization precession frequency at position (x, z) . ρ denotes the magnetization distribution. C_m represents the spatial distribution of the sensitivity for the m^{th} coil. $\Delta\omega$ is the bandwidth per read-out pixel, ω_0 is the resonance frequency. R is the domain containing the imaging object. The index $l = 1, \dots, L$ indicates the l^{th} frequency step, while $n = 1, \dots, N$ indicates the n^{th} rotation.

Note that the magnetization precession frequency $\omega(x, z)$ depends on the spatial distribution of the magnetic field strength $b(x, z)$: $\omega(x, z) = \gamma_b(x, z)$, where γ is the gyromagnetic ratio. According to Maxwell's equations, a linear magnetic field in the z direction generated by gradient coils must have nonzero x and y field components (13–15). In fact, this physical principle causes significant concomitant-field artifacts in low-field and ULF MRI (13–15). Thus, the total magnetic field $\mathbf{b}(x, z)$ experienced by the magnetization is

$$\mathbf{b}(\mathbf{r}) = \mathbf{b}_{\text{ideal}}(\mathbf{r}) + \mathbf{b}_{\text{con}}(\mathbf{r}), \quad [2]$$

with the ideal magnetic field

$$\mathbf{b}_{\text{ideal}}(\mathbf{r}) = (B_0 + \mathbf{g}^T \mathbf{r}) \mathbf{e}_z, \quad [3]$$

where B_0 is the main field and $\mathbf{g} = [g_x \ g_y \ g_z]^T$ is the ideal linear magnetic field gradient for spatial encoding. The concomitant field is approximately

$$\mathbf{b}_{\text{con}}(\mathbf{r}) = (-g_z x/2 + g_x z) \mathbf{e}_x + (-g_z y/2 + g_y z) \mathbf{e}_y, \quad [4]$$

where \mathbf{e}_x , \mathbf{e}_y , and \mathbf{e}_z are unit vectors along the axes of the Cartesian coordinate system.

Because our current RSA implementation is for 2D imaging, we assume, without losing generality, that $g_y = 0$ and $y = 0$ in the subsequent formulation.

We first want to express the similarity between RSA and the use of radial k-space trajectories in high-field MRI, where the concomitant fields can be neglected. If the RSA frequency-encoding magnetic field is ideally linear along the x axis, the magnetic field strength (x, z) is

$$b_{\text{ideal}}(x, z) = B_0 + g_x x, \quad [5]$$

To further facilitate the comparison, we use a new coordinate system (\tilde{x}, \tilde{z}) fixed to the imaging object: $\tilde{x} = x \cos(\theta_n) + z \sin(\theta_n)$ and $\tilde{z} = -x \sin(\theta_n) + z \cos(\theta_n)$. Eq. [1] is thus re-written as

$$S_{\text{RSA}}^m(\omega_l, \theta_n) = \int_{\mathbf{R}} \rho(\tilde{x}, \tilde{z}) C_m(\tilde{x} \cos(\theta_n) - \tilde{z} \sin(\theta_n), \tilde{x} \sin(\theta_n) + \tilde{z} \cos(\theta_n)) \text{sinc}\left(\frac{\tilde{x} \cos(\theta_n) - \tilde{z} \sin(\theta_n) - (l - L/2)\Delta d}{\Delta d}\right) d\tilde{x} d\tilde{z}, \quad [6]$$

where $\Delta d = \Delta\omega/\gamma g_x$ is the nominal spatial resolution. Here we assume that the magnetization precesses at frequency ω_0 at the center of the FOV.

Comparison of RSA and Radial Trajectory Acquisition

In high-field MRI acquisition using radial k-space trajectories (11), the combination of x and z gradients is used to generate a projection onto a line, which rotates around the origin at an angle θ_n , which varies between 0 and 2π across repetitions. The magnetic field strength $b(x, z)$ is $B_0 + x \cos(\theta_n) g_x - z \sin(\theta_n) g_z$

$$S_{\text{radial}}^m(\omega_l, \theta_n) = \int_{\mathbf{R}} \rho(x, z) C_m(x, z) \text{sinc}\left(\frac{x \cos(\theta_n) - z \sin(\theta_n) - (l - L/2)\Delta d}{\Delta d}\right) dx dz. \quad [7]$$

Equations [6] and [7] show the similarity between the RSA and data acquisition using a radial k-space trajectories when ignoring concomitant-field artifacts. Note that the difference between Eqs. [6] and [7] is that the coil sensitivity varies across rotations in RSA, but remains invariant across rotations in radial trajectory acquisition. When using only one receiving coil with uniform coil sensitivity, these two methods produce identical data. Furthermore, if receiving coils with identical sensitivity distributions are arranged circularly symmetrically around the imaging object with a separation between coils by angle $\Delta\theta$, and there exists a permutation function $f_n(m)$ such that the incremental angle used in RSA and radial acquisition are related to each other by $C_m(x \cos(\theta_n) - z \sin(\theta_n), x \sin(\theta_n) + z \cos(\theta_n)) = C_{f_n(m)}(x, z)$ for each n , then RSA and radial-trajectory acquisition are equivalent: $S_{\text{RSA}}^m(\omega_l, \theta_n) = S_{\text{radial}}^{f_n(m)}(\omega_l, \theta_n)$, because the total

information collected from all coils and all rotating angles are the same.

However, when considering the concomitant field, RSA and radial k-space trajectory acquisition are in fact quite different. Using a radial k-space trajectory, the magnetic field strength $b(x, z)$, including the concomitant field, is $\sqrt{[B_0 + x \cos(\theta_n)g_x^{\max} + z \sin(\theta_n)g_z^{\max}]^2 + [-x \sin(\theta_n)g_z^{\max} + z \cos(\theta_n)g_x^{\max}]^2}$. Clearly, $b(x, z)$ varies across readouts of different rotating angles θ_n . Consequently, the spatial distribution of the resonance frequency at θ_n is not simply rotating the distribution of the resonance frequency at θ_n degree by $(\theta_n - \theta_m)$. Additionally, during a radial k-space trajectory in ULF MRI, the magnetic field experienced by magnetization located at (x, z) is $(B_0 + x \cos(\theta_n)g_x^{\max} + z \sin(\theta_n)g_z^{\max})\mathbf{e}_z + (-x \sin(\theta_n)g_z^{\max}/2 + z \cos(\theta_n)g_x^{\max})\mathbf{e}_x$. This suggests that the orientation of the magnetic field, and thus the magnetization precession axis, changes at every acquisition angle. These two features pose the technical challenge of calibrating the distribution of resonance frequencies accurately at each projection angle to reconstruct the image with minimal artifacts, including image blurring and distortion. The use of RSA, where the image object is rotated without changing the spatial-encoding magnetic fields, can directly avoid these two challenges as described above.

From Eq. [4], the magnetic field strength (x, z) , including the concomitant field, is equal to $\sqrt{(B_0 + xg_x)^2 + (zg_x)^2}$, which varies nonlinearly along the x direction. However, this magnetic field is invariant across rotating angles. Accordingly, if image reconstruction can explicitly incorporate the field distribution, the blurring arising from concomitant fields can be reduced significantly. Different from conventional ULF MRI, in which both frequency and phase encoding are used to produce an image, RSA requires no phase encoding, thus simplifying the image reconstruction without the necessity of considering highly nonlinear phase increments across phase-encoding steps because of different precession axes, precession frequencies, and initial angles (15). The absence of phase encoding also allows acquisition very soon after the prepolarizing pulse, before significant T_2 decay has taken place.

Image Reconstruction

To reconstruct an image with resolution Δd , we assume that the magnetization is constant within a $\Delta d \times \Delta d$ square region centered at (x_μ, z_ν) and that these discrete spatial points (x_μ, z_ν) are separated by Δd along x and z directions. Equation [6] can be re-written as a linear equation with a spatial encoding matrix \mathbf{A} , entries of which can be calculated by numerical integration of Eq. [6], an unknown magnetization distribution \mathbf{x} including all $\rho(x_\mu, z_\nu)$ at discretized points, and the measured signal in frequency domain \mathbf{b} . To solve this equation, Tikhonov regularization (16) is used to suppress noise amplification corresponding to small eigenvalues of the encoding matrix :

$$\mathbf{x} = \arg \min_{\mathbf{x}} (||\mathbf{Ax} - \mathbf{b}||_2^2 + \lambda ||\mathbf{Dx}||_2^2) \quad [8]$$

where λ is a regularization parameter and \mathbf{D} is the matrix of a difference operator along x and z directions.

METHODS

Simulations

To compare the performance of RSA, radial k-space trajectory acquisition, and Cartesian trajectory acquisition, we simulated data acquisitions from an MRI system with eight receiving coils. Simulations included no concomitant field. Coil sensitivities were simulated based on experimental measurements using one $21 \text{ mm} \times 21 \text{ mm}$ pick-up coil of a SQUID. Prepolarization at a 20-mT field with 4-s duration was used to ensure sufficient SNR in the coil sensitivity measurement (further experimental detail follow). Specifically, eight maps of coil sensitivity were generated by rotating the measured coil sensitivity with 45° increments. In the first simulation, the 2D image grid was 128×128 . For each acquisition method, we reconstructed data with full sampling, $R=1$, which refers to using an incremental rotation of $360^\circ/128$ of the object in RSA, $360^\circ/128$ incremental rotation of the gradient vector in radial trajectory acquisition, and 128 phase encoding steps in Cartesian trajectory acquisition with the resolution and FOV matched to RSA and radial trajectory acquisition. Additionally, we also simulated two- and four-fold accelerations ($R=2$ and 4) to compare the performance of different imaging strategies under acceleration. Furthermore, to investigate how the number of sensors affects the quality of a reconstructed image, we reconstructed images using one, two, four, and eight receiver channels. The sensors were placed circumferentially around the imaging volume as evenly as possible. In the simulation, complex Gaussian noise was added to the data. We adjusted the noise level such that the ratio between the center of the k-space data and the standard deviation of the noise in k-space was the same as in the experimental data. This noise level was considered as the 100% noise level in our study. RSA and radial trajectory-data were reconstructed by the Conjugate Gradient Squared method (17) to solve Eq. [8] iteratively. The regularization parameter was manually adjusted such that the boundary of the image reconstructed from the fully sampled RSA data became visually as sharp as the fully sampled SENSE reconstruction. This λ was considered as the 100% regularization. We used the same λ in both RSA and radial k-space trajectory acquisition in different accelerations and with different numbers of receiving coils. Cartesian trajectory acquisition data were reconstructed by the SENSE method (18).

To compare how the image quality changes at different spatial resolutions, we also reconstructed images using simulated data acquired by RSA, radial trajectory, and Cartesian trajectory with only one single receiver with a 64×64 2D image grid.

The simulations above did not consider the effect of concomitant field. To demonstrate that RSA is able to reduce the concomitant artifact, we first simulated signals acquired with a strong concomitant field using RSA and a Cartesian trajectory without noise. Eight receiving coils and an 128×128 image grid without acceleration was used as our first simulation. The main magnetic field was $50 \text{ } \mu\text{T}$ and the frequency-encoding gradient (1 mT/m) was constantly kept on. For the Cartesian trajectory simulation, the maximal phase-encoding gradient

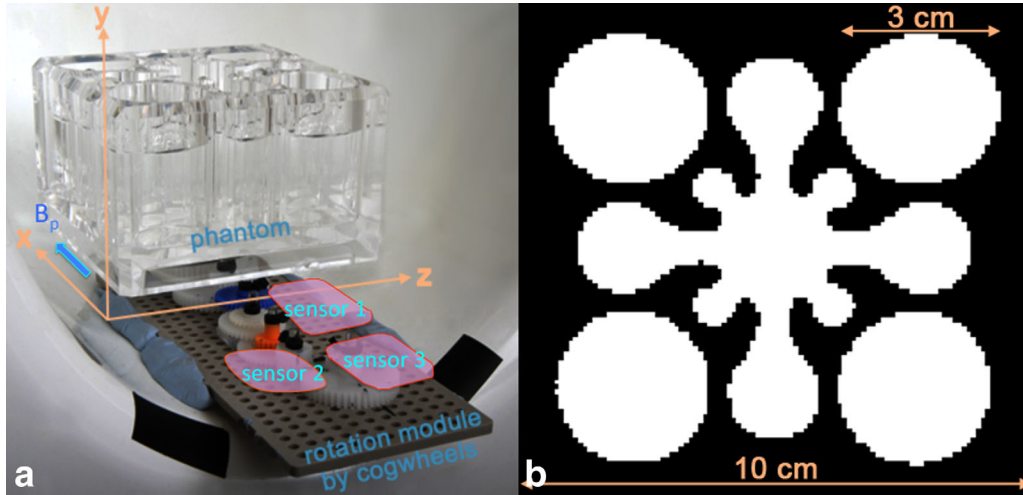


FIG. 1. Experimental setup (A), where B_p denotes the direction of the prepolarization field, and the outline of the phantom (B) measured at 3T.

strength was 1 mT/m. The effect of the concomitant field was quantified as ϵ , the maximal gradient field strength times the FOV (10×10 cm) divided by the main magnetic field strength (14). ϵ was 2 in this simulation. ULF signals were simulated by taking the numerical integration over the FOV using a 1024×1024 grid in the image domain. For the Cartesian trajectory, images were constructed by first Fourier transforming each receiving coil image and then taking the square root of the sum-of-squares images. For RSA, images were reconstructed using Eq. [8] without and with correct precession frequency information, respectively. To demonstrate that RSA can work with only one receiving coil and to investigate how the image quality is affected by the noise and regularization, we performed another simulation, where images were reconstructed using a simulated one-receiving-coil data set with 100%, 31.6%, and 10% noise levels. These images used 100%, 10%, and 1% of the regularization, respectively.

Experiment

Figure 1 shows the experimental setup, including the relative positions of three sensors and the rotation module with cogwheels for rotating a square phantom, and the cross section image of a saline phantom on a 3 tesla (T) MRI scanner. All experiments were done on the ULF-MRI system at Aalto University. The noise floor of the SQUID sensors was 4–5 fT/ $\sqrt{\text{Hz}}$. Note that an ULF-MRI sensor consisted of a pick-up coil coupled to a SQUID. The SQUID is a tiny device transforming magnetic flux to voltage. In our experiment, we used three magnetometer 21 mm \times 21 mm loops as the pick-up coils. Details of this system have been published previously (5). In the ULF-MRI experiments, the magnetization was generated by a 20-mT prepolarization field for 4 s. The prepolarization field was then turned off adiabatically, and a standard spin-echo pulse sequence was used to sample ULF-MRI data at 10 kHz for 250 ms ($TE=300$ ms and $TR=4.5$ s). The main magnetic field was 50 μT and the frequency-encoding gradient (50 $\mu\text{T/m}$) was kept on

constantly. Note that our system had a rather weak concomitant field ($\epsilon=0.1$). We used no phase encoding. The phantom was rotated by 3.36° between readouts. In total, we collected 106 readouts for one fully sampled RSA. The measurement was performed 9 times. To match the number of acquisitions using a Cartesian trajectory (see below), 100 measurements were randomly selected from 106 RSA readouts in each average. The data acquisition time for nine repetitions in one projection was 40.5 s. It took roughly 15 s to rotate the imaging object manually by 3.36° . Taken together, the total imaging time was approximately 93 min to collect the data set of 100 projections and 9 acquisitions per projection. The same amount of data (number of phase-encoding lines times the number of acquisitions) was used to collect the Cartesian trajectory data.

For comparison, we also acquired ULF-MRI data using a Cartesian raster trajectory with 10 acquisitions, each of which included 90 phase-encoding steps. The maximal phase-encoding gradient strength was 75 $\mu\text{T/m}$. The duration of the phase-encoding gradient was 80 ms. This allowed us to achieve approximately 2×2 mm² spatial resolution. Fourier-encoded data were reconstructed by the SENSE method. A total of 900 readouts were made for both RSA and Cartesian-trajectory data. To investigate the performance of image reconstruction using accelerated acquisitions, we also reconstructed images with 50% (50 rotation angles with nine acquisitions in RSA; 45 equally spaced Cartesian k-space lines with phase encoding with 10 acquisitions; $R=2$) and 33% (34 rotation angles with 9 averages in RSA; 30 equally spaced Cartesian k-space lines with phase encoding with 10 acquisitions; $R=3$) of fully sampled data.

Coil sensitivities were estimated as a least-squares fit of a 3rd-order polynomial to the phantom image. The diameter of the circular water phantom was 11.2 cm. The phantom images were acquired 10 times using Cartesian trajectories. We estimated the noise level of each receiving coil by calculating the standard deviation of data points at 30 frequency-encoding lines near the resonance frequency ω_0 (2250 Hz) but without explicit

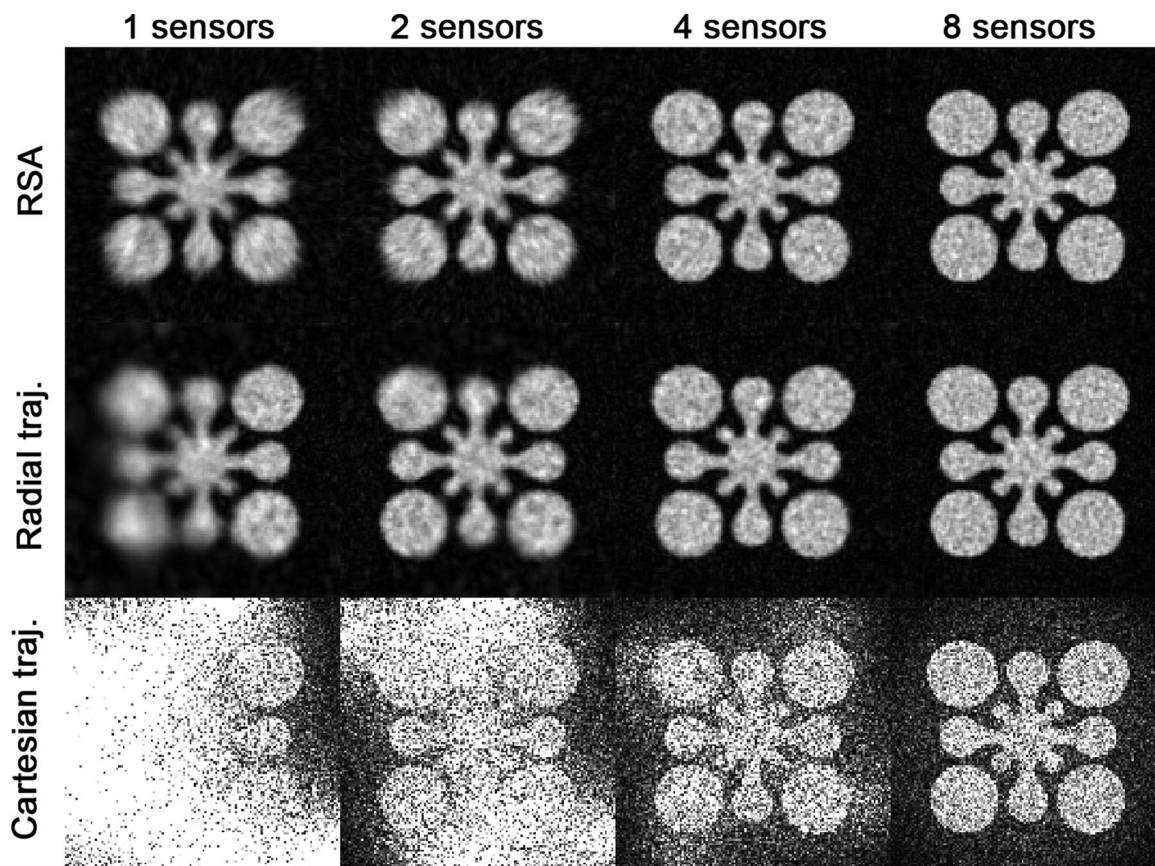


FIG. 2. Simulation images reconstructed from data collected by RSA, radial trajectory acquisition, and Cartesian trajectory acquisition using one, two, four, and eight sensors with no concomitant field ($\epsilon = 0$).

phantom signal. The magnetic field was first mapped using a fluxgate magnetometer (Mag-03MC, Bartington Instruments, Oxon, UK) with 1.6×1.6 cm resolution and then spatially filtered by a second-order polynomial fit to obtain a map of resonance frequency.

RESULTS

Figure 2 shows the reconstructed images in simulations using RSA, radial trajectory acquisition, and Cartesian-trajectory acquisition with one, two, four, and eight receiving coils without any concomitant field. With only one receiving coil (close to the upper right corner of the image), RSA shows a symmetric blurring artifact around the imaging object. Also radial-trajectory images have blurring artifacts, particularly at voxels away from the position of the receiving coil. Cartesian-trajectory acquisition led to a noisy and partially reconstructed image near the position of the receiving coil. As the number of sensors was increased, the noise level and the blurring artifacts in images reconstructed from RSA and radial trajectory acquisition both decreased. In images reconstructed from Cartesian-trajectory acquisitions, increasing the number of sensors decreased the noise level. Still, the images had much higher noise than those reconstructed by RSA and radial-trajectory acquisition. Compared with images reconstructed from data using

Cartesian-trajectory acquisition, RSA and radial-trajectory acquisition can generate images with less noise.

Figure 3 shows the reconstructed images using RSA, radial-trajectory acquisition, and Cartesian-trajectory acquisition using eight receiving coils at one-, two-, and four-fold accelerations without any concomitant field. As expected, the image quality decreased with increasing acceleration factor. However, images reconstructed from RSA and radial-trajectory acquisition still have visually discernible outline of the saline phantom at four-fold acceleration. The noise level of the reconstructed images using a Cartesian-trajectory acquisition increased dramatically for two- and four-fold accelerations.

Figure 4 shows simulation images reconstructed from Cartesian-trajectory acquisition, RSA, and radial-trajectory acquisition with 64×64 and 128×128 image matrix using a single receiving coil without a concomitant field. Using Cartesian-trajectory acquisition, the SNR at 128×128 resolution was lower than at 64×64 resolution, because the signal dropped to $1/4$ ($1/4$ voxel size) while the standard deviation of the noise only dropped to $1/2$ (four-fold data samples with the assumption of homogeneous noise power at the k-space). Interestingly, when using RSA and radial trajectory acquisition, we found that the SNR at the higher spatial resolution (128×128) is higher than at the lower spatial resolution (64×64). This is likely because of denser sampling near

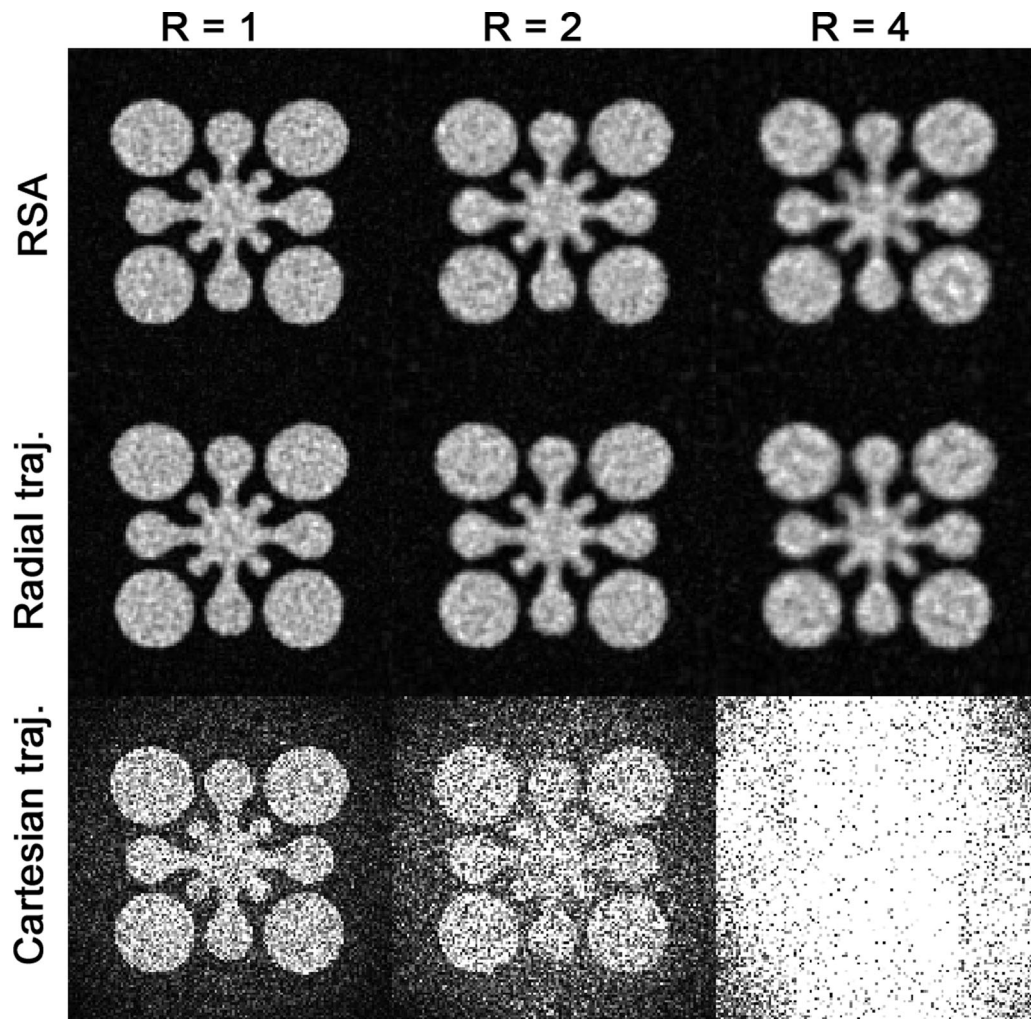


FIG. 3. Simulation images reconstructed from data collected by RSA, radial trajectory acquisition, and Cartesian trajectory acquisition at one-, two-, and four-fold accelerations with no concomitant field ($\epsilon = 0$).

the center of the k-space and the regularized reconstruction algorithm.

Figure 5A shows the spatial distribution of the precession frequency during readout when a strong concomitant field was present ($\epsilon = 2$). Figure 5B shows the image reconstructed from a Cartesian trajectory. We observed serious blurring at the top and the bottom of the image. Figure 5C shows the image reconstructed from RSA without considering the concomitant field. The image was blurred over the whole FOV, but the shape of the phantom still can be recognized. Figure 5D shows the image reconstructed from RSA with explicit consideration of the concomitant field. It has no blurring artifact.

Figure 6 shows RSA images reconstructed with only one receiving coil with 100%, 31.6%, and 10% noise level in a strong concomitant field ($\epsilon = 2$). A sharper image was reconstructed because a lower regularization was used. Interestingly, the reconstructed image shows minimal blurring at the 10% noise.

Figure 7 shows the spatial distribution of the magnetization precession frequency measured in our ULF-MRI system ($\epsilon = 0.1$). We observed that, as expected, the

spatial distribution of the precession frequency was not perfectly linear, particularly at the left side of the image.

Figure 8 shows images reconstructed separately from three sensors from the experimental data with RSA and Cartesian sampling. Cartesian sampling produced localized SNR enhancement close to the position of the pickup coil. Using RSA, each sensor produced an image showing the overall profile of the saline phantom. We found that experimental images were similar to simulation results (Fig. 4). It is worth noting that the blurring artifact (particularly the blurring direction) in each receiving coil image is different. This suggested the possibility of reducing image blurring artifact by combining data across receiving coils.

Figure 9 shows the reconstructed images with one, two, or three receiving coils using RSA and SENSE for Cartesian data. As the number of receiving coils increased, the combined reconstruction showed gradually reduced image blurring. The SENSE reconstruction had the least noise around the sensor but failed to reconstruct voxels further away from the receiving coils (the upper-left corner of the image). In the SENSE images, the

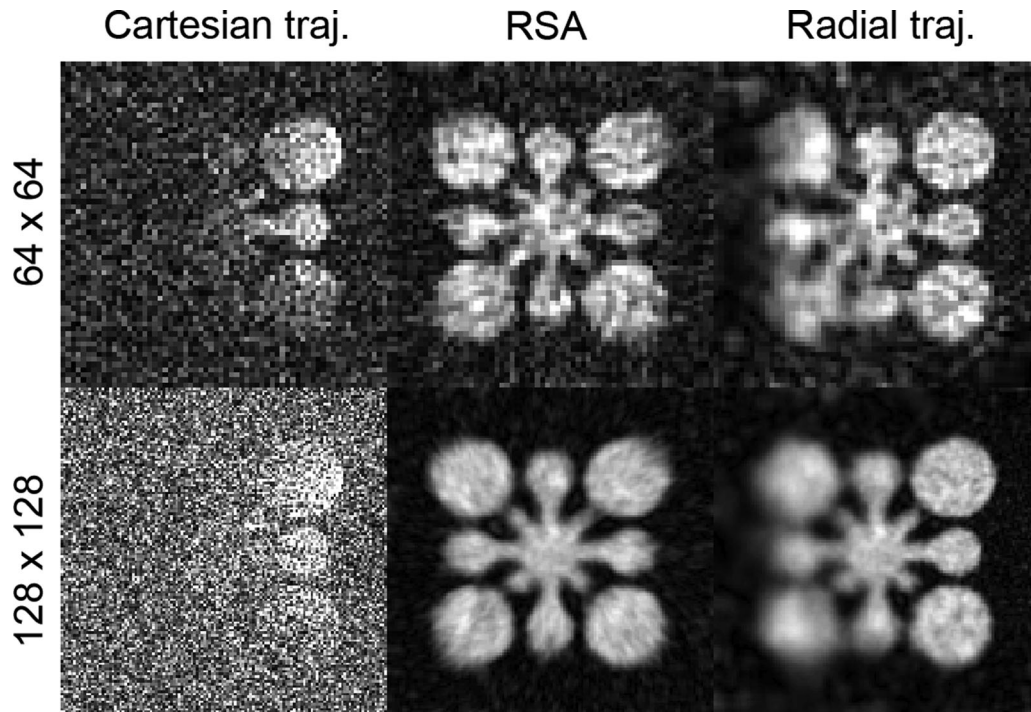


FIG. 4. Simulated single-sensor images reconstructed from data collected by Cartesian trajectory acquisition, RSA, radial trajectory acquisition using lower (64×64 image matrix) and higher (128×128 image matrix) resolutions with no concomitant field ($\varepsilon=0$).

phantom is only marginally visible at the lower right corner of the image at two-fold acceleration, disappearing completely in the noise at three-fold acceleration. Even at three-fold acceleration, RSA generated a good phantom image, regardless of whether one, two, or three receiving coils were used.

DISCUSSION

In this study, we proposed the RSA method and demonstrated it in an ULF-MRI system. First, we showed that RSA and radial-trajectory acquisition are theoretically similar but practically different (see THEORY section). Using simulations, we demonstrated that both methods produce images with similar and reduced blurring artifacts when more than four sensors were used (Fig. 2). Using both simulations and empirical data, we demonstrate that the RSA method is more efficient than Cartesian sampling in reconstructing a full-FOV image with

only a few (three) receiving coils (Figs. 3 and 9). In the presence of a strong concomitant field, our simulations demonstrated that RSA has only a minimal blurring artifact (Figs. 5 and 6). It can even reconstruct a reasonable phantom image with only 33% of fully sampled data, where 100% fully Fourier-encoded data using Cartesian trajectory can only produce an image showing part of the phantom (Figs. 2, 8, and 9). However, the tradeoff is the lower SNR close to receiving coils than with SENSE reconstruction using Cartesian k-space sampling (Fig. 9).

It should be noted that, in ULF MRI, the implementation of radial trajectories is complicated by the fact that combinations of gradient coils for producing different readout directions cause variable concomitant fields over the course of data acquisition (see the Theory section). Consequently, reconstructing ULF MRI from radially sampled data requires careful characterization of the magnetic field for all acquisition angles θ_n to accurately reconstruct images of optimal quality. Such a task can be

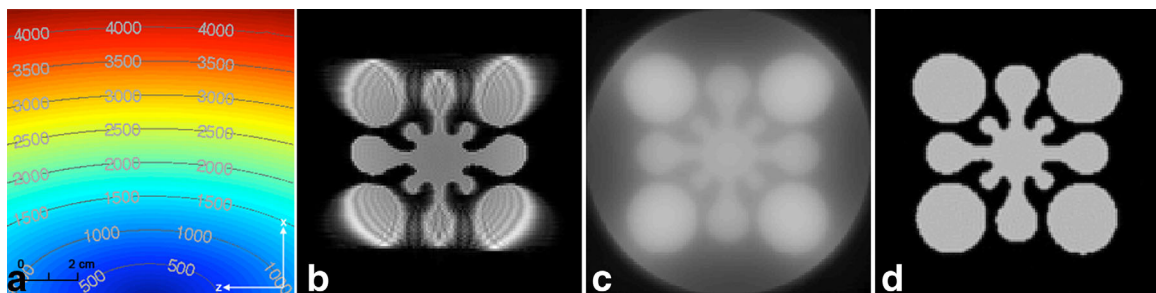


FIG. 5. **A:** spatial distribution of the precession frequency during readout. **B:** The reconstructed image using a Cartesian trajectory and eight receiving coils. **C:** The reconstructed image using RSA and eight receiving coils at a strong concomitant field ($\varepsilon=2$) with moderate noise. **D:** The reconstructed image using RSA and eight receiving coils at a strong concomitant field ($\varepsilon=2$) with low noise.

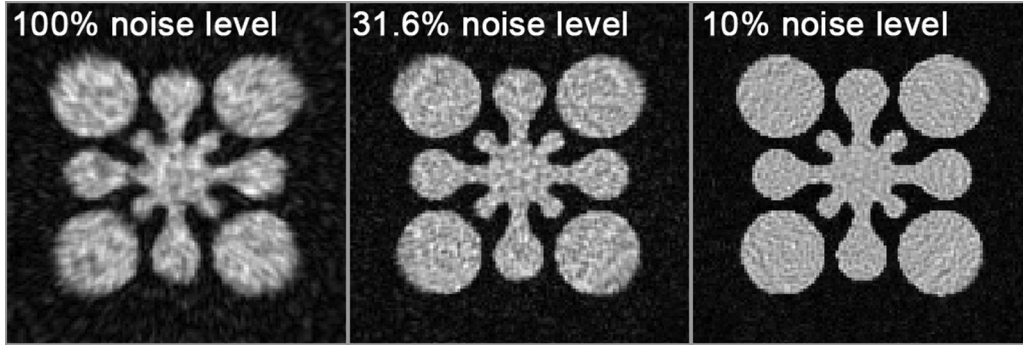


FIG. 6. Simulated images reconstructed from one receiving coil data collected by RSA with 100%, 31.6%, and 10% noise at a strong concomitant field ($\epsilon = 2$).

tedious. Importantly, RSA only requires one magnetic-field map, which includes the gradient and concomitant field. Consequently, RSA is a simpler approach than radial-trajectory acquisition in ULF MRI.

One interesting feature of RSA is that different receiving coils show blurring artifacts along different directions (Fig. 10). This can be explained by the fact that (i) blurring occurs along the iso-resonance-frequency direction, and (ii) each receiving coil dominantly measures the NMR signal close to itself. The blurring direction in a given voxel is thus determined by the orientation of the iso-resonance-frequency direction with respect to the phantom when the voxel is close to the sensor. The final reconstructed RSA images therefore include all blurring directions over the rotation in RSA (Fig. 10).

We would like to clarify that RSA actually can generate an image without any blurring using only one receiving coil, when the coil sensitivity is known and the noise is small. This was demonstrated in Figure 6. However, considering noise contamination in a practical experimental setup, the reconstruction from single-channel data shows significant blurring (Fig. 6), which is the consequence of the necessary regularization to

stabilize the image-encoding matrix inverse in image reconstruction. Using data from multiple channels at the same noise level can further improve the condition of the image-encoding matrix. Consequently, the reconstruction shows even less blurring (Fig. 2).

Note that a magnetic field gradient is required in RSA. This is different from fast MRI approaches of using highly parallel detection and minimal gradient encoding (19). The fundamental difference between our approach and fast MRI was directly shown in Figure 6, where an image of minimal blurring can be reconstructed using data from only one channel. This is impossible for methods of spatial encoding using no gradient but coil sensitivity.

Under the constraint of sampling the same region of k-space, increasing the sampling evenly across readouts in a Cartesian trajectory is known to cause image resolution enhancement and consequently image voxel SNR degradation, when the noise is assumed homogeneous across k-space. However, both simulated (Fig. 3) and experimental demonstrations (Figs. 8 and 9) suggest that RSA and radial trajectory acquisition may increase the SNR as the spatial resolution is increased. This may be explained by the k-space sampling density and the fact that most natural objects have large low-spatial-frequency signals. With Cartesian sampling, as the image resolution increased from 64×64 to 128×128 , the sampled k-space region was extended two-fold in each

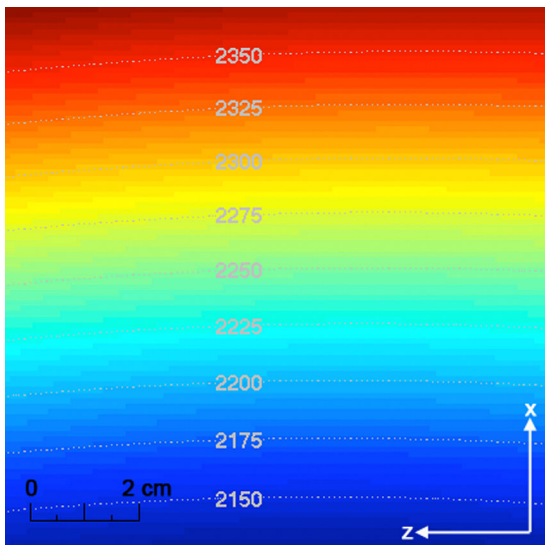


FIG. 7. The spatial map of the Larmor precession frequency in Hz with a weak concomitant field ($\epsilon = 0.1$).

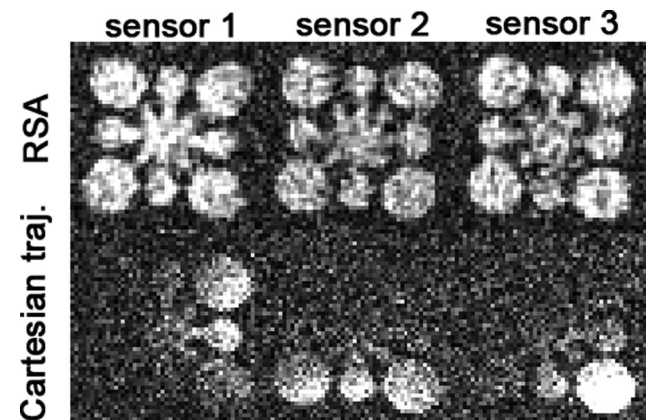


FIG. 8. Experimental single-sensor images reconstructed from data collected by RSA and Cartesian sampling.

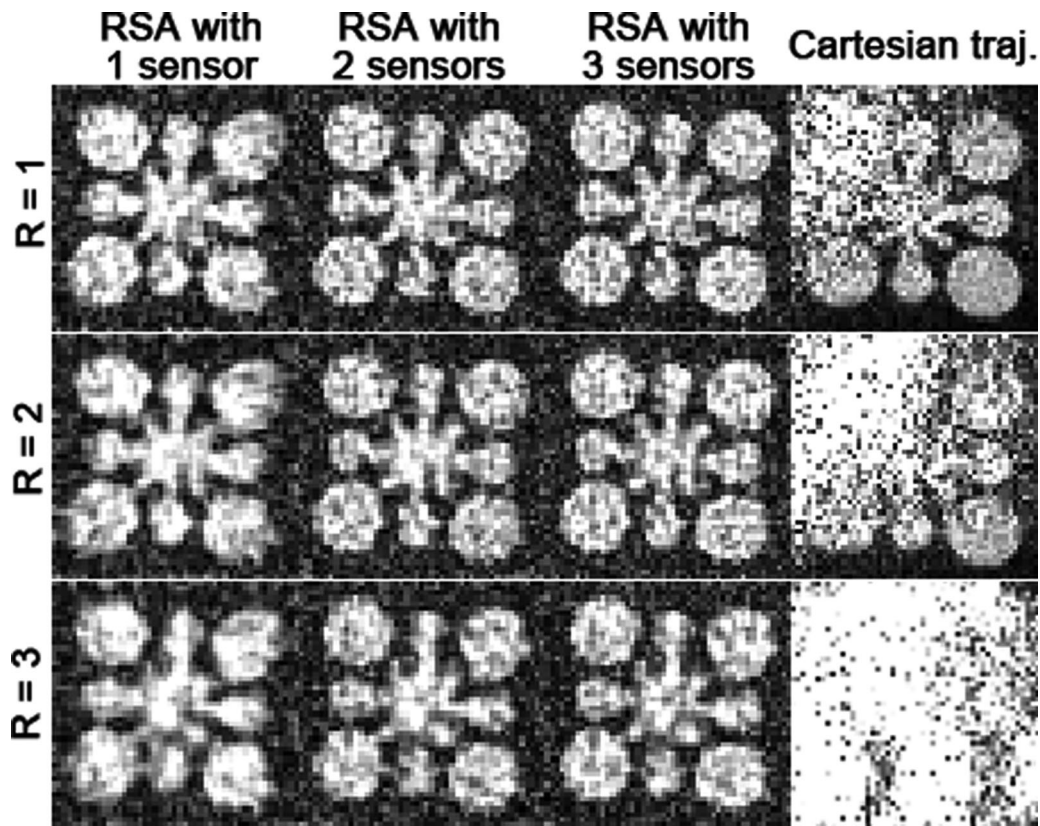


FIG. 9. Experimental combined images reconstructed from data collected by RSA and Cartesian trajectory acquisition using one, two, and three sensors at one-, two-, and three-fold acceleration. For comparison, SENSE reconstructions using Cartesian sampling are shown in the right-most column.

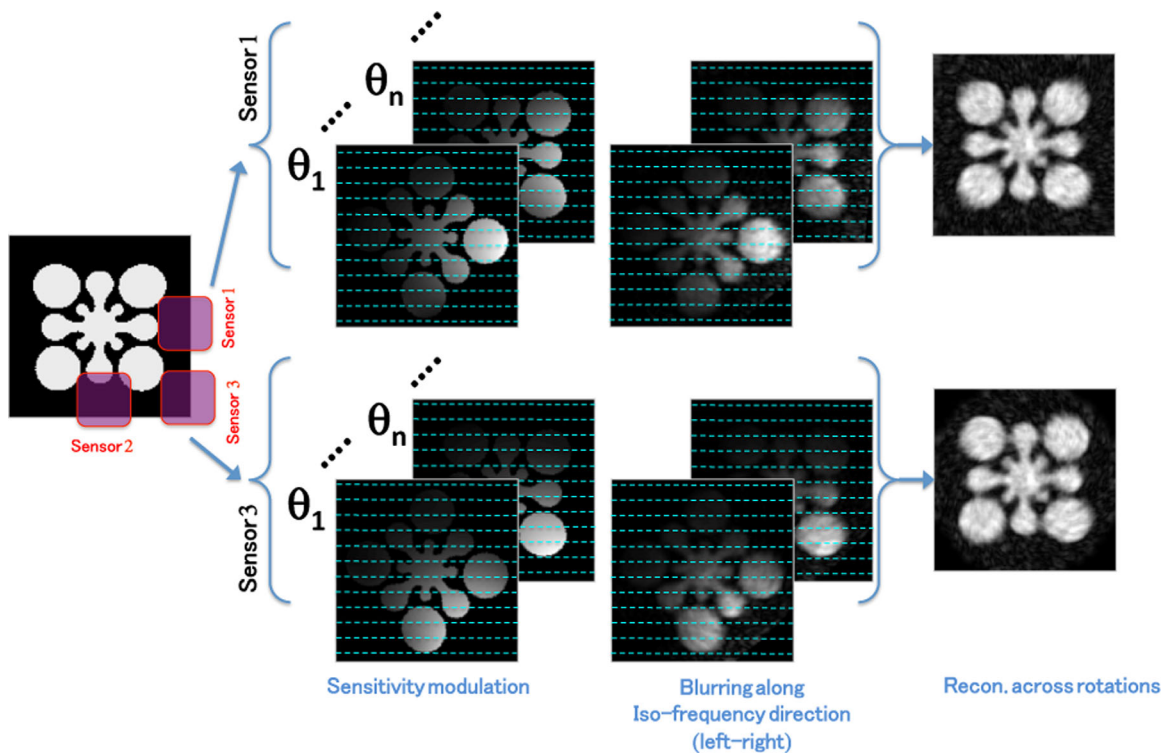


FIG. 10. Graphical illustration of image distortions in RSA across rotations for sensors 1 and 3. Cyan dashed lines indicate iso-resonance-frequency contours. The blurring direction in a given voxel is mostly determined by the orientation of the iso-resonance-frequency direction with respect to the phantom when the voxel is close to the sensor.

k-space dimension with the same sampling density. For RSA and radial trajectory acquisition, both the sampled k-space region and the sampling density are changed. Particularly, the sampling density at the lower-spatial-frequency region is doubled. This is helpful in delineating naturalistic objects with high density in low-spatial-frequency components and may explain why the image quality is better in higher-resolution simulation images (128×128 versus 64×64 image matrix; Figures 2 and 3). In fact, these observations were supported by experimental images (Fig. 8).

In RSA, we reduced concomitant field artifacts by explicitly describing the relationship between magnetization and measured signal under imaging gradient fields and concomitant field (14,15). There are other approaches to minimize the concomitant field artifacts. For example, generating an effectively unidirectional gradient field can use Fourier transform to reconstruct images (20,21). Comparing with these approaches, our method uses a simpler acquisition at the cost of more complex computations in image reconstruction.

The RSA method proposed here resembles the approach by Kelso et al (21), where the imaging object was rotated during data acquisition. However, there is a significant difference: The approach by Kelso et al used only one receiver with a rather homogeneous sensitivity. Data were processed as those from a radial k-space trajectory, and images were reconstructed by the filtered back-projection algorithm. In contrast, our approach uses multiple channels. Importantly, we suggest that these two methods are only equivalent when using only one receiving coil with constant coil sensitivity (see the Comparison of RSA and Radial Trajectory Acquisition subsection in the THEORY section). This difference was also demonstrated in simulations (Fig. 2).

While we demonstrated the feasibility of RSA in an ULF-MRI system, we expect that RSA can also work in other experimental setups. This is subject to three conditions: (i) there is a static magnetic field capable of encoding spatial information; (ii) the sample or the whole instrument, including all gradient coils and receivers, can rotate stably; and (iii) the coil sensitivity is invariant (or known) when the sample or the instrument rotates. One possible example of such a system is a low-field MRI system (22). Therefore, RSA may be a useful method in low-field, low-weight, or portable MRI.

REFERENCES

1. Vaughan JT, Garwood M, Collins CM, et al. 7T vs. 4T: RF power, homogeneity, and signal-to-noise comparison in head images. *Magn Reson Med* 2001;46:24–30.
2. Clarke J, Hatridge M, Mölle M. SQUID-detected magnetic resonance imaging in microtesla fields. *Annu Rev Biomed Eng* 2007;9:389–413.
3. Fischer HW, Rinck PA, van Haverbeke Y, Muller RN. Nuclear relaxation of human brain gray and white matter: analysis of field dependence and implications for MRI. *Magn Reson Med* 1990;16:317–334.
4. Busch S, Hatridge M, Mölle M, Myers W, Wong T, Mück M, Chew K, Kuchinsky K, Simko J, Clarke J. Measurements of T1-relaxation in ex vivo prostate tissue at 132 μ T. *Magn Reson Med* 2012;67:1138–1145.
5. Vesanen PT, Nieminen JO, Zevenhoven KCJ, et al. Hybrid ultra-low-field MRI and MEG system based on a commercial whole-head neuro-magnetometer. *Magn Reson Med* 2013;69:1795–1804.
6. Magnelind PE, Gomez JJ, Matlashov AN, Owens T, Sandin JH, Volegov PL, Espy MA. Co-registration of interleaved MEG and ULF MRI using a 7 channel low-Tc SQUID system. *IEEE Trans Appl Supercond* 2011;21:456–460.
7. McDermott R, Trabesinger AH, Mück M, Hahn EL, Pines A, Clarke J. Liquid-state NMR and scalar couplings in microtesla magnetic fields. *Science* 2002;295:2247–2249.
8. Norris DG, Hutchison JMS. Concomitant magnetic-field gradients and their effects on imaging at low magnetic-field strengths. *Magn Reson Imaging* 1990;8:33–37.
9. Volegov PL, Mosher JC, Espy MA, Kraus RH Jr. On concomitant gradients in low-field MRI. *J Magn Reson* 2005;175:103–113.
10. Yablonskiy DA, Sukstanskii AL, Ackerman JJH. Image artifacts in very low magnetic field MRI: the role of concomitant gradients. *J Magn Reson* 2005;174:279–286.
11. Lauterbur PC. Image formation by induced local interactions. Examples employing nuclear magnetic resonance. *Clin Orthop Relat Res* 1973;242:190–191.
12. Block KT, Uecker M, Frahm J. Undersampled radial MRI with multiple coils. Iterative image reconstruction using a total variation constraint. *Magn Reson Med* 2007;57:1086–1098.
13. Myers WR, Mossle M, Clarke J. Correction of concomitant gradient artifacts in experimental microtesla MRI. *J Magn Reson* 2005;177:274–284.
14. Nieminen JO, Ilmoniemi RJ. Solving the problem of concomitant gradients in ultra-low-field MRI. *J Magn Reson* 2010;207:213–219.
15. Hsu Y-C, Vesanen PT, Nieminen JO, Zevenhoven KCJ, Dabek J, Parkkonen L, Chern IL, Ilmoniemi RJ, Lin F-H. Efficient concomitant and remanence field artifact reduction in ultra-low-field MRI using a frequency-space formulation. *Magn Reson Med* 2014;71:955–965.
16. Hansen PC, O'Leary DP. The use of the L-curve in the regularization of discrete ill-posed problems. *SIAM J Sci Comput* 1993;14:1487–1503.
17. Sonneveld P. CGS, a Fast Lanczos-type solver for nonsymmetric linear systems. *SIAM J Sci Stat Comp* 1989;10:36–52.
18. Pruessmann KP, Weiger M, Scheidegger MB, Boesiger P. SENSE: sensitivity encoding for fast MRI. *Magn Reson Med* 1999;42:952–962.
19. Lin FH, Wald LL, Ahlfors SP, Hämäläinen MS, Kwong KK, Belliveau JW. Dynamic magnetic resonance inverse imaging of human brain function. *Magn Reson Med* 2006;56:787–802.
20. Bouchard L-S. Unidirectional magnetic-field gradients and geometric-phase errors during Fourier encoding using orthogonal ac fields. *Phys Rev B* 2006;74:054103.
21. Kelso N, Lee S-K, Bouchard L-S, Demas V, Mück M, Pines A, Clarke J. Distortion-free magnetic resonance imaging in the zero-field limit. *J Magn Reson* 2009;200:285–290.
22. Colley LL, Stockmann JP, Armstrong BD, Sarraçanie M, Rosen MS, Wald LL. Two-dimensional imaging in a lightweight portable MRI scanner without gradient coils. *Magn Reson Med* 2015;73:872–883.